Pergamon

Geochimica et Cosmochimica Acta, Vol. 66, No. 3, pp. 507–519, 2002

0016-7037/02 $22.00 + .00

PII S0016-7037(01)00784-0

Ar and K partitioning between clinopyroxene and silicate melt to 8 GPa

E. M. Chamorro,[1,†] R. A. Brooker,[1,*] J.-A. Wartho,[2,‡] B. J. Wood,[1] S. P. Kelley,[2] and J. D. Blundy[1]

[1]CETSEI, Department of Earth Sciences, University of Bristol, Wills Memorial Building, Queens Road, Bristol, BS8 1RJ, United Kingdom
[2]Department of Earth Sciences, Open University, Walton Hall, Milton Keynes, MK7 6AA, United Kingdom

(*Received October* 4, 2000; *accepted in revised form July* 30, 2001)

Abstract—The relative incompatibility of Ar and K are fundamental parameters in understanding the degassing history of the mantle. Clinopyroxene is the main host for K in most of the upper mantle, playing an important role in controlling the K/Ar ratio of residual mantle and the subsequent time-integrated evolution of $^{40}Ar/^{36}Ar$ ratios. Clinopyroxene also contributes to the bulk Ar partition coefficient that controls the Ar degassing rate during mantle melting. The partitioning of Ar and K between clinopyroxene and quenched silicate melt has been experimentally determined from 1 to 8 GPa for the bulk compositions $Ab_{80}Di_{20}$ (80 mol% albite–20 mol% diopside) and $Ab_{20}Di_{80}$ with an ultraviolet laser ablation microprobe (UVLAMP) technique for Ar analysis and the ion microprobe for K. Data for Kr (UVLAMP) and Rb (ion probe) have also been determined to evaluate the role of crystal lattice sites in controlling partitioning. By excluding crystal analyses that show evidence of glass contamination, we find relatively constant Ar partition coefficients (D_{Ar}) of 2.6×10^{-4} to 3.9×10^{-4} for the $Ab_{80}Di_{20}$ system at pressures from 2 to 8 GPa. In the $Ab_{20}Di_{80}$ system, D_{Ar} shows similar low values of 7.0×10^{-5} and 3.0×10^{-4} at 1 to 3 GPa. All these values are several orders of magnitude lower than previous measurements on separated crystal-glass pairs.

D_K is 10 to 50 times greater than D_{Rb} for all experiments, and both elements follow parallel trends with increasing pressure, although these trends are significantly different in each system studied. The D_K values for clinopyroxene are at least an order of magnitude greater than D_{Ar} under all conditions investigated here, but D_{Ar} appears to show more consistent behavior between the two systems than K or Rb. The partitioning behavior of K and Rb can be explained in terms of combined pressure, temperature, and crystal chemistry effects that result in changes for the size of the clinopyroxene M2 site. In the $Ab_{20}Di_{80}$ system, where clinopyroxene is diopside rich at all pressures, D_K and D_{Rb} increase with pressure (and temperature) in an analogous fashion to the well-documented behavior of Na. For the $Ab_{80}Di_{20}$ system, the jadeite content of the clinopyroxene increases from 22 to 75 mol% with pressure resulting in a contraction of the M2 site. This has the effect of discriminating against the large K^+ and Rb^+ ions, thereby countering the effect of increasing pressure. As a consequence D_K and D_{Rb} do not increase with pressure in this system.

In contrast to the alkalis (Na, K, and Rb), D_{Kr} values are similar to D_{Ar} despite a large difference in atomic radius. This lack of discrimination (and the constant D_{Ar} over a range of crystal compositions) is also consistent with incorporation of these heavier noble gases at crystal lattice sites and a predicted consequence of their neutrality or "zero charge." Combined with published D_{Ar} values for olivine, our results confirm that magma generation is an efficient mechanism for the removal of Ar from the uppermost 200 km of the mantle, and that K/Ar ratios in the residuum are controlled by the amount of clinopyroxene. Generally, Ar is more compatible than K during mantle melting because D_{Ar} for olivine is similar to D_K for clinopyroxene. As a result, residual mantle that has experienced variable amounts of melt extraction may show considerable variability in time-integrated $^{36}Ar/^{40}Ar$.

1. INTRODUCTION

Noble gas geochemistry has long been recognized as a powerful tool in understanding accretion and the evolutionary history of the Earth, including the formation of the atmosphere and crust (e.g., Harmano and Ozima, 1978; Ozima and Podosek, 1983; Allègre et al., 1987; Jambon, 1994; Harper and Jacobsen, 1996; Coltice et al., 2000). Isotope ratios, particularly of He and Ar, have been used to infer the presence of various steady state geochemical reservoirs, the most important being a deep, relatively isolated, and undegassed mantle that is rich in primordial noble gases (Hart et al., 1985; Allègre et al., 1987, 1996; Turner, 1989; Porcelli and Wasserburg, 1995; O'Nions and Tolstikhin, 1996). Recently, this simple layered structure with isolation of an undepleted lower mantle has been questioned because geophysical imaging indicates that subducted slabs penetrate deep into the lower mantle (e.g., van der Hilst et al., 1997), because numerical models of whole mantle convection suggest that preservation of a laterally extensive primordial reservoir is unlikely (van Keken and Ballentine, 1999), and because evidence from other trace elements suggests that the lower mantle is generally "processed" to some extent, rather than primordial (e.g., Hofmann, 1997).

As the primordial status of the lower mantle is increasingly questioned, new chemical geodynamic models are being developed to explain observed noble gas systematics (e.g., Anderson, 1993; Coltice and Ricard, 1999; Phipps-Morgan and Morgan, 1999). Even basic constraints, such as the bulk earth K content and the nature of accreted noble gases, are being

* Author to whom correspondence should be addressed (r.a.brooker@bristol.ac.uk).
† *Present address:* Ecole Normale Supérieure de Lyon, Laboratoire de Géologie, 46 Allée d'Italie, 69364 Lyon Cedex 07, France.
‡ *Present address:* School of Applied Geology, Curtin University, GPO Box U1987, Perth WA 6001, Australia.

reassessed (Davies, 1999; Ozima and Igarashi, 2000). To evaluate or develop these more complex models, it is important to establish the physicochemical processes that might control the distribution of noble gases and any parental nuclides throughout the mantle.

It is generally accepted that degassing of the Earth (and the other terrestrial planets) arises from melting at depths corresponding to the upper mantle, with partitioning of gas into the melt, followed by ascent, exsolution, and degassing to the atmosphere (e.g., Broadhurst et al., 1990). The most important factors controlling these processes are the bulk partition coefficients (D_i = crystal/melt weight concentration ratio of element i) that describe how noble gases are distributed between crystals and melt in the source region. Models that attempt to describe Earth degassing and formation of the atmosphere are highly dependent on assumptions related to these coefficients (e.g., Zhang and Zindler, 1989; McKenzie and O'Nions, 1991), and in some cases on the relative compatibilities of Ar and K (e.g., Harmano and Ozima, 1978; Coltice et al., 2000). Although these models generally assume noble gases to be highly incompatible ($D_i \ll 1$), some early experimental studies have suggested that this is not the case, with partitioning approaching compatible behavior at both low pressure (Broadhurst et al., 1990, 1992) and (inferred) at higher pressures, greater than 4 to 5 GPa (Chamorro-Perez et al., 1996, 1998). These observations, if correct, would require dramatic revision of the current models for the Earth's degassing history, as based on noble gases.

Although bulk D values depend on the residual mineralogy during melting, clinopyroxene is particularly important as it is the only mineral to contain a large lattice site (M2) capable of accommodating a wide range of large ions including Na^+, K^+, and Rb^+. Consequently, clinopyroxene has a profound influence on the incompatible trace element chemistry of mantle melts and residues. Because the atomic radius of Ar is similar to the ionic radius of K^+ and the relative compatibilities of K and Ar are directly reflected in time-integrated parent (^{40}K)–daughter (^{40}Ar) ratios, clinopyroxene might be expected to play an important role in understanding relationships between degassing and ingrowth of radiogenic/primordial Ar isotope systematics (i.e., $^{40}Ar/^{36}Ar$)

Experimental measurements of olivine and clinopyroxene melt partition coefficients for noble gases (Hiyagon and Ozima, 1982, 1986; Broadhurst et al., 1990, 1992; Shibata et al., 1994; Brooker et al., 1998a) and studies of natural crystal-melt pairs (Batiza et al., 1979; Kurz et al., 1982; Kaneoka et al., 1983; Marty and Lussiez, 1993; Valbracht et al., 1994) have resulted in a wide range of partition coefficients (more than three orders of magnitude for Ar) from highly incompatible ($D_i \ll 1$) to compatible ($D_i > 1$), with an apparent increase in compatibility with increasing size of the noble gas atom (Hiyagon and Ozima, 1986; Broadhurst et al., 1992). Brooker et al. (1998a) have suggested that much of this variability is related to problems with experimental and analytical methods, most of which can be avoided (or at least limited) by a microprobe technique such as the ultraviolet laser ablation microprobe (UVLAMP). By this method, Brooker et al. (1998a) demonstrated that Ar is highly incompatible in clinopyroxene grown from a melt in a 0.1-MPa Ar atmosphere. However, these preliminary results were themselves subject to considerable uncertainty because of the low concentrations of Ar dissolved in the crystals at 0.1 MPa. The presence of relatively Ar-rich melt inclusions in the product crystals is a particular problem because these are difficult to avoid when the relatively large ablation pit size required to analyze such low Ar concentrations are used.

To constrain noble gas partitioning behavior and the resultant K/Ar ratios, the present study was designed to measure D_K and D_{Ar} between clinopyroxene and silicate melt equilibrated over a range of conditions (pressures of 1 to 8 GPa, temperatures up to ~1800°C), where Ar solubility in the melt may potentially exceed 40,000 ppm. Variation of the clinopyroxene composition, along with additional measurements for D_{Kr} and D_{Rb}, provides important information on the relationship between crystal sites and noble gas size. The relatively high concentrations of noble gas requires only small pit sizes and takes full advantage of the microprobe technique to produce more precise measurements of partition coefficients. High concentrations also act to minimize any possible influence of dislocations, or extended defects (e.g., grain boundaries), which may explain the high disequilibrium partition coefficients obtained in some studies (see Brooker et al., 1998a). The use of a simple synthetic system has many experimental advantages (see below). Furthermore, the more simplified crystal chemistry allows the control of lattice sites to be more clearly illustrated. This important aspect is discussed briefly in this study, but a more complete evaluation (including partitioning data for an additional 16 trace elements) will be presented elsewhere.

2. EXPERIMENTAL AND ANALYTICAL TECHNIQUES

2.1. Starting Materials

The new experiments performed for this study used a glass starting composition 80 mol% albite and 20 mol% diopside ($Ab_{80}Di_{20}$). Because we were unable to find a published phase diagram related to this system at the higher pressures of this study, several experiments were designed to constrain the liquidus phases and temperatures (Table 1). As expected, this composition has clinopyroxene as a liquidus phase from low to high pressure. In addition, the melt compositions are known to form glass (without quench devitrification) in high-pressure experiments and also have a high noble gas solubility (as predicted from the model of Carroll and Stolper, 1993).

In addition to the new experiments, several experimental charges from the studies of Blundy and Wood (1994) and Blundy et al. (1995) in the system $Ab_{20}Di_{80}$, containing euhedral clinopyroxene surrounded by areas of quench devitrification and clear glass, were analyzed by UVLAMP (Table 1). In these experiments, Ar was loaded either as a contaminant from air (in pore space and adsorbed onto surfaces) or from the Ar gas stream used during capsule welding. Major and trace element data for one further, previously unpublished experiment in the $Ab_{20}Di_{80}$ system (BW17) are included in this study.

The $Ab_{80}Di_{20}$ starting composition was prepared from oxides and carbonates. The starting mixture was decarbonated and then melted in a platinum crucible at 1350°C. The resulting glass was doped with a cocktail of trace elements (including 422 ppm K) to a total concentration of 0.7 wt%, then remelted (at 1300°C) and reground through a number of cycles. The composition of this starting material is confirmed by analysis of superliquidus glasses in high-pressure experiments as follows: SiO_2 64.80; Al_2O_3 15.33; MgO 3.61; CaO 5.19; and Na_2O 9.67 (average of 60 analyses in wt%). The doped glass was then loaded into open platinum capsules and saturated in noble gases by melting at 1300°C at 0.1 GPa in a TZM cold-seal pressure vessel with an equimolar mixture of He, Ne, Ar, and Kr gases as the pressure medium.

The quench rate for the $Ab_{80}Di_{20}$ starting material melted at 0.1 GPa was not rapid enough to prevent the formation of numerous quench clinopyroxene crystals, and the high viscosity also resulted in the

Table 1. Experimental run conditions and products.

Run	Apparatus	P (GPa)	T (°C)	Cooling rate	Run time (h)	Run products[a]
$Ab_{80}Di_{20}$ samples						
98PC3	PC	2.0	1850[b]–1336	1°C/min	2.5	L + cpx
98PC4	PC	2.0	1415–1336	1°C every 3 min	4.0	L + cpx
98PC1	PC	2.1	1500–1475	1°C/min	19.5	L
98PC2	PC	2.1	1470–1400	1°C/min	15.3	L + cpx
99PC7	PC	2.7	1500–1475	1°C/min	1.0	L
99PC8	PC	2.7	1475–1425	1°C every 2 min	14.7	L + cpx
99PC11	PC	3.6	1500–1475	1°C every 10 min	2.0	L
99PC12	PC	3.6	1475–1450	1°C every 5 min	1.0	L + cpx (di-core)
99PC13	PC	3.7	1500–1460	1°C every 5 min	1.0	L + cpx
99PC14	PC	3.7	1515–1460	1°C every 2 min	4.0	L + cpx
99PC15	PC	3.7	1495–1475–1455	Cycled	1.5	L + cpx
99PC16	PC	3.7	1475[b]	NA	20.0	L + cpx
99MA4	MA	4.7	1625–1565	Single step	1.0	L + cpx (di-core)
99MA1	MA	5.6	1700[b]	NA	0.7	L + cpx + co
99MA6	MA	5.6	1700–1650	Single step	1.3	L + cpx
99MA2	MA	8.1	1685–1660	Single step	1.0	L + cpx + co
99MA3	MA	8.1	1815–1765	Single step	1.3	L + cpx
99MA7	MA	8.1	1700–1630	Single step	1.3	L + cpx + co
$Ab_{20}Di_{80}$ samples						
93PC11[c]	PC	1.0	1390	NA	6.0	L + cpx
93PC26[c]	PC	3.0	1665	NA	2.7	L + cpx
93MA1[c]	MA	6.0	1765	NA	0.2	L + cpx
BW17	MA	12.0	2050	NA	0.3	L + cpx

[a] co = coesite; cpx (di-core) = cpx with diopside cores; cpx = clinopyroxene; L = melt; MA = multi anvil press; NA, not applicable. PC = end-loaded piston cylinder.
[b] Estimated temperature (broken thermocouple).
[c] Samples from study of Blundy et al. (1995).

retention of some gas bubbles. For the subsequent high-pressure experiments, the 0.1-GPa glass was first homogenized by grinding it into a fine powder. Next, it was loaded into platinum capsules (1.8 mm in diameter and typically 3 mm in length), which were then sealed by welding. Details of the preparation of the $Ab_{20}Di_{80}$ starting glass can be found in Blundy et al. (1995).

2.2. Experimental Techniques

All experiments (except BW17) were performed at the University of Bristol. Experimental conditions and products are described in Table 1. For most experiments in this study, the temperature was first increased above that of the liquidus to dissolve any residual low-pressure crystals and then slowly decreased to the final conditions (Table 1 for cooling procedures). All the samples were quenched by shutting off the electrical power; quench rates are in excess of 150°C s^{-1} for the initial 1000°C.

The 1- to 4-GPa experiments were performed in an end-loaded piston cylinder apparatus with $BaCO_3$ cells and W/Re_3-W/Re_{25} thermocouples. The temperature difference between the sample and the thermocouple has been measured as ≤15°C (Blundy et al. 1995). The 5- to 8-GPa experiments were carried out in a Walker-type multianvil press (Walker et al., 1990). The assembly consisted of an MgO (Ceramcast) octahedron (containing 5 wt% Cr_2O_3) with an edge length of 18 mm, a $LaCrO_3$ heater, and a ZrO_2 sleeve between furnace and octahedron. Temperature was monitored with a W-Re axial thermocouple. Pressure was increased at room temperature, and the sample was then heated to the required temperature. Temperature uncertainties are greater than in the piston–cylinder apparatus but still appear to be within ±20°C (Blundy et al. 1995). Although the original intention was to measure the partition coefficients for all the noble gases loaded into the starting material, it was soon discovered that He concentrations in the high-pressure experiments were far below that in the loaded starting glass. This was taken to indicate that He was escaping through the platinum capsule wall, as observed for other small radii atoms (e.g., Brooker et al., 1998b). The Ne concentrations were a little lower than expected in the starting glass but appeared to be reduced further in some experiments. As a result, we were unable to obtain reliable partitioning data for the lighter gases. The Ar concentrations in the high-pressure experiments are greater than the starting glass (see Results for an explanation), whereas the measured Kr is consistent with the loaded concentration. It is assumed that both Ar and Kr are retained within the platinum capsule due to their large size.

The 12-GPa BW17 experiment was performed in a split-sphere multianvil apparatus at the University of Bayreuth, and the sample was loaded into an unwelded Re capsule. This unsealed experiment was not designed to measure Ar partitioning, but data for major and trace elements are presented.

2.3. Analytical Methods

Recovered samples were sectioned and polished with alumina paste before characterization by scanning electron microscopy for texture and compositional zonation. Major element compositions of phases were determined via Cameca and JEOL electron microprobes in WDS mode with standard procedures to eliminate Na loss during analysis (see Blundy et al., 1995). Fresh surfaces were then exposed for UVLAMP analysis.

For the UVLAMP analysis, carried out at the Open University, Milton Keynes, UK, a pulsed quadrupled Nd:YAG laser (λ = 266 nm) with a pulse duration of 10 ns, a repetition rate of 10 Hz, and a beam diameter of ~10 μm was either rastered over square regions (25 to 100 μm^2) ablating 1.4 to 28 μm per layer, or employed in 8- to 28-μm-wide straight-line rasters of varying length (~5 to 13 μm deep). A Märzhäuser MAC 4000 computerized X-Y stage, attached to a customized Leica DMR microscope, was used to control the raster speed (20 μm s^{-1}) and the size of the laser pit. The laser beam size and shape was adjusted with an Optics for Research beam expander to give good ablation, forming a flat-based laser pit. Raster times were typically 3 and 10 min for melt and crystal, respectively. The noble gas isotopes released after the ablation of each layer were "gettered" with 3 SAES NP10 getters and analyzed with a high-sensitivity mass spectrometer (MAP 215-50). Further details regarding the mass spectrometer and the ultraviolet laser technique can be found in Kelley et al. (1994), Brooker

Table 2. Chemical analyses of selected run products.[a]

	$Ab_{80}Di_{20}$ samples									Brooker et al. (1998a)	$Ab_{20}Di_{80}$ samples		
Run	98PC2	98PC3	98PC4	99PC8	99PC13	99MA1	99MA6	99MA3	99MA7	BDHB-2Di	93PC11[b]	93PC26[b]	BW17
Pressure (GPa)	2.1	2.0	2.0	2.7	3.7	5.6	5.6	8.1	8.1	0.1 MPa	1.0	3.0	12.0
T (°C)	1470–1400	1850–1336[c]	1415–1336	1475–1425	1500–1460	1625[c]	1700–1650	1685–1660	1700–1630	1285	1390	1665	2050
Pyroxene													
No. of analyses	20	10	10	10	10	21	10	37	19	10	36	22	15
SiO_2	56.09 (50)	55.51 (60)	56.33 (135)	55.73 (56)	56.62 (33)	58.28 (49)	56.36 (48)	58.59 (40)	57.26 (49)	54.55 (24)	55.05 (20)	56.77 (21)	55.91 (52)
Al_2O_3	9.00 (32)	6.86 (40)	8.60 (86)	10.23 (27)	14.76 (52)	19.61 (28)	18.69 (25)	19.54 (44)	20.05 (42)	1.79 (14)	0.74 (10)	1.35 (12)	4.06 (14)
MgO	13.70 (34)	15.47 (36)	13.00 (106)	13.14 (38)	9.38 (54)	5.93 (30)	7.07 (31)	5.49 (27)	5.55 (64)	20.31 (22)	18.98 (19)	19.58 (15)	17.13 (25)
CaO	16.96 (21)	19.47 (38)	16.73 (143)	16.33 (20)	11.28 (58)	7.03 (25)	8.17 (25)	6.17 (33)	6.66 (35)	23.37 (16)	23.77 (18)	23.20 (18)	20.75 (15)
Na_2O	4.33 (23)	3.02 (14)	4.63 (71)	5.24 (15)	7.65 (51)	9.68 (26)	9.34 (25)	10.45 (23)	10.88 (46)	0.14 (08)	0.31 (28)	0.59 (43)	2.10 (6)
Total[d]	100.08	100.37	99.28	100.57	99.68	100.53	99.65	100.24	100.40	100.16	98.85	101.49	99.95
Glass													
No. of analyses	8	10	10	14	20	16	10	8	15	20	17	197	36
SiO_2	66.35 (17)	65.90 (54)	64.50 (80)	65.46 (43)	67.93 (41)	70.35 (40)	66.98 (41)	69.92 (27)	68.27 (45)	54.66 (30)	56.44 (35)	57.01 (28)	50.86 (95)
Al_2O_3	15.91 (7)	15.79 (17)	15.50 (29)	15.83 (26)	15.23 (10)	11.86 (45)	14.17 (22)	11.19 (22)	9.83 (17)	14.13 (10)	6.88 (12)	4.17 (15)	4.50 (18)
MgO	3.12 (4)	3.02 (12)	3.02 (8)	2.96 (15)	2.34 (9)	2.10 (26)	2.50 (8)	2.21 (5)	1.22 (8)	12.21 (11)	11.32 (19)	14.75 (57)	16.74 (49)
CaO	4.78 (4)	4.56 (14)	4.76 (10)	4.59 (16)	3.81 (14)	4.38 (12)	4.46 (16)	4.57 (4)	4.71 (9)	16.96 (13)	17.45 (14)	20.65 (33)	19.15 (30)
Na_2O	9.17 (12)	9.27 (18)	10.70 (32)	10.13 (51)	9.45 (38)	8.74 (24)	8.95 (17)	9.08 (14)	9.36 (18)	0.74 (21)	4.09 (13)	2.48 (20)	2.04 (11)
Trace elements[d]						1.67	1.12	1.55	4.53	—	1.35	0.93	5.31
Total	99.03	98.58	98.48	98.98	98.76	99.10	98.18	98.46	98.72	98.70	97.53	99.99	98.60
Na cpx/melt	0.47	0.32	0.43	0.52	0.81	1.11	1.04	1.15	1.16	0.19	0.07	0.24	1.03
Estimated cpx wt%	4	5	5	5	28	48 (+co)	25	49	53 (+co)	25	45	7	65

[a] Values in parentheses are 1 standard deviation.
[b] Data from Blundy et al. (1995).
[c] Estimated temperature (broken thermocouple).
[d] A limited selection of trace elements were analyzed for certain melts. Where analyzed, crystals contained ~0.1 wt% trace elements.

et al. (1998a), and Wartho et al. (1999). Representative blanks for 3-min runs obtained during the experiments are as follows: $^{40}Ar = 5 \times 10^{-12}$, $^{36}Ar = 9 \times 10^{-14}$ and $^{84}Kr = 5 \times 10^{-14}$ cm^3 STP.

To determine the volumes of ablated material and hence calculate concentrations of argon in the sample, laser pit depths were measured with a noncontact vertical scanning interferometer (an RST Plus at John Moores University, Liverpool, UK), which has a precision of ~1 Å. Melt densities were calculated using Lange and Carmichael (1987), and crystal density estimated from Deer et al. (1992) was used to convert the values (to STP cm^3 g^{-1} or wt% ppm). Errors quoted for the Ar concentrations reflect uncertainty in the analytical measurements (generally ±0.5%, but these can be as high as ±50% for very low concentrations), measurement of laser pit dimensions (±0.5 μm), and density estimates (5 and 10% for the melt and crystals, respectively).

The K and Rb concentrations in crystals and glass were obtained with the Cameca IMS-4f ion microprobe at the University of Edinburgh following procedures described in Blundy and Wood (1994).

2.4. Attainment of Equilibrium

Although the experiments of this study are not reversed, studies aimed at measuring rare earth elements, Th, and U partitioning between clinopyroxene and liquid (Blundy and Wood, 1994; Blundy et al., 1998; Landwehr et al., 2001) conducted under similar conditions produced crystals that were unzoned with respect to trace elements. Furthermore, trace element partition coefficients in those experiments follow the parabolic dependence on ionic radius predicted for equilibrium partitioning by Nagasawa (1966) and Brice (1975). Additional support for equilibration of the noble gases is given by the calculation of Hiyagon and Ozima (1986), who used conservative estimates of noble gas diffusion coefficients in melt to show that a 200-μm crystal that grew in 1 min should remain in equilibrium. Given that most of our experiments (Table 1) were cooled slowly, growing crystals in 25 to 4800 min, disequilibrium due to rapid crystal growth is extremely unlikely. It will be demonstrated that our measured partition coefficients indicate Henrian behavior (i.e., they are independent of concentration) for a wide range of crystal Ar contents (10^{-5} to 10^{-1} ppm) and that the observed partitioning behavior of Ar and Kr are consistent with incorporation at lattice sites. Both these factors suggest that equilibrium was attained.

3. RESULTS

The phases present in each experimental charge are listed in Table 1. Major element analyses of selected experimental run products are reported in Table 2. For experiments that use the $Ab_{20}Di_{80}$ starting composition, the clinopyroxene is >79 mol% diopside end member over the entire pressure range, with minor amounts of enstatite (<13%), jadeite (<8%), and <3% CaTs. For $Ab_{80}Di_{20}$ experiments the jadeite component increases markedly with pressure, from 21% at 2 GPa to 72% at 8 GPa. Enstatite is consistently <10% and CaTs < 10%. At 5 to 8 GPa, coesite is also a stable phase at subliquidus temperatures (Table 1).

Clinopyroxenes were generally euhedral and varied in length from 10 μm to several hundred microns, with the largest being produced in the multianvil experiments (Fig. 1 and Table 3). Although melt generally quenched to a homogeneous glass, patches of fine-textured devitrification were observed in some (notably multianvil) experiments. Such patches were more extensive for the $Ab_{20}Di_{80}$ compositions. Where possible, devitrified areas were avoided during analysis, but for sample 93PC11, both glass and devitrified areas were analyzed extensively to determine the effects of quench modification on Ar retention. The results of this comparison are included in Table 3. The error that results from the range of concentration in the devitrified regions is generally much larger than for the glass

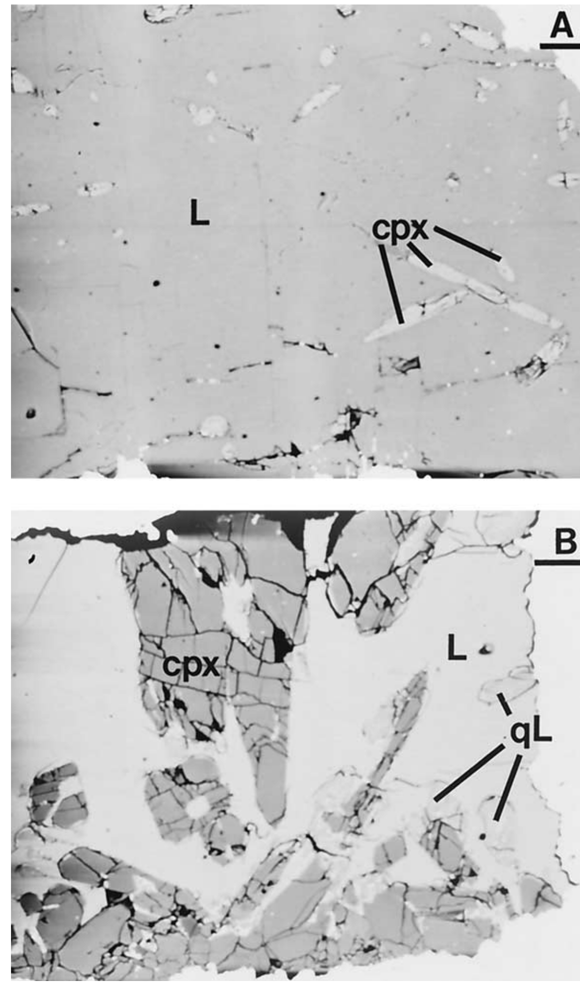

Fig. 1. Backscattered electron images of experimental charges (A) 98PC2 and (B) 99MA3 showing the different crystal morphologies and typical dimensions for low- and high-pressure experiments of this study. L = glass; qL = devitrified glass; cpx = clinopyroxene. Scale bar = 100 μm.

(for 93PC11, the range is 233 to 930 ppm for devitrified areas compared with 428 to 748 ppm Ar for the vitreous glass). The averages of 10 analyses are, however, the same within uncertainty, at 599 and 529 ppm Ar, respectively. Thus, devitrified quenched liquid can be used to determine D_{Ar}, provided that a sufficient number of analyses are obtained to assess the standard deviation. This is an important result given the difficulty of producing glass from experiments on basaltic compositions at pressures greater than 2 GPa.

Figure 2 shows the Ar contents of glasses as a function of pressure (Table 3) compared with two models for the solubility limit of Ar in the melt. Model A was calculated from the ionic porosity model of Carroll and Stolper (1993) and assuming Henry's Law behavior. Model B follows the same curve to 5 GPa, thereafter taking account of a potential change in distribution of "hole" size, which would reduce solubility at higher pressures as suggested by Chamorro-Perez et al. (1998). Both models imply that all melts were undersaturated in Ar at the conditions of the experiment so that Ar-rich fluid inclusions could not have produced spurious results. Furthermore, the Ar

Table 3. Ar and Kr concentrations.

Sample	Crystal description	Pressure (GPa)	Crystal concentration in ppm (group A and B in Fig. 3): Average (n)[a]	Error[b]	Lowest	Highest	Melt concentration (ppm): Average (n)	Error[b]	Range
Ar in $Ab_{80}Di_{20}$ samples									
98PC4	Very small and thin (max 50 μm long)	2.0	2.64 (6)	±1.21	0.9	4.25	248 (22)	±78	127–381
98PC2	Thin and long (30 × 300 μm)	2.1	—	—	—	—	484 (9)	±190	246–834
98PC8	Very small and thin (max, 50 μm long)	2.7	—	—	—	—	553 (4)	±77	447–658
99PC16	Small and skeletal (max 100 μm long)	3.7	0.88 (1)	±0.01	—	—	397 (5)	±99	277–560
99MA1	Large (up to 100 × 500 μm)	5.6	0.36 (4)	±0.16	0.19	0.57	719 (7)	±113	556–880
99MA3	One large crystal (100 × 300 μm)	8.1	0.51 (6)	±0.32	0.18	0.85	612 (5)	±44	538–671
							648 (2)	*±73*	*575–721*
Kr in $Ab_{80}Di_{20}$ samples									
99MA6	Large (up to 100 × 500 μm)	5.6	0.021 (3)	±0.006	0.013	0.026	51 (6)	±9	42–64
99MA7	Large (up to 100 × 500 μm)	8.1	0.099 (8)	±0.094	0.014	0.198	128 (2)	±6	121–134
Ar in $Ab_{20}Di_{80}$ samples									
BDHB-2Di[c]	Large (1800 × 500 μm) with long, thin melt inclusions	0.0001	9.4×10^{-5} (2)	$\pm 3.3 \times 10^{-4}$	8.3×10^{-5}	0.0010	0.103 (7)	±0.009	0.095–0.111
93PC11	Large euhedral (200 × 500 μm)	1.0	0.050 (2)	±0.01	0.04	0.06	599 (9)	±85	428–747
							529 (10)	*±240*	*233–931*
93PC26	Long and thin but euhedral (50 × 200 μm)	3.0	0.072 (2)	±0.004	0.068	0.076	243 (8)	±20	200–265

Melt values in italic are for devitrified glass analyses.
[a] n = number of analyses in unweighted means.
[b] Includes UVLAMP instrumental error, pit measurement, and density uncertainty.
[c] Also including data of Brooker et al. (1998a).

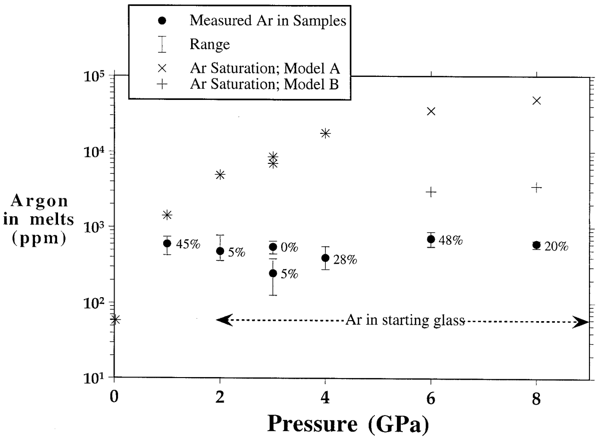

Fig. 2. Argon concentrations in silicate melts. All $Ab_{80}Di_{20}$ experimental samples of this study and samples 93PC11 and 93PC26 from Blundy et al. (1995) have Ar contents above that predicted for the loaded starting material (corrected for the degree of crystallization, as indicated by % next to the data point). The Blundy et al. (1995) samples (marked 45 and 5%) were made from a nominally Ar-free starting material but contained similar amounts of Ar in relation to other experiments. All samples are shown to be undersaturated at run pressures, regardless of the method used to calculate solubility. Model A uses data from Carroll and Stolper (1993); model B is after Camorro-Perez et al. (1998) for pressures greater than 5 GPa (see text). The Di-rich sample BDHB-2Di, which is not shown, has an Ar melt content at sub–parts per million levels.

contents of the glasses are invariably much higher than the concentration in the starting glass that was saturated with the noble gas mixture at 0.1 GPa (Ar concentration predicted to be ~60 ppm with the model of Carroll and Stolper, 1993). These results indicate that some Ar was introduced to the capsule, probably during TIG welding in an argon gas stream. This suggestion is entirely consistent with the observation that 93PC11 and 93PC26 (from Blundy et al., 1995) have concentrations of Ar similar to our experimental charges, even though this starting material was not preloaded with Ar (Fig. 2). Calculations suggest that only 0.015 to 1.5 ppm Ar can be loaded if air-filled pore spaces represent 0.5 to 50% of the capsule volume (see results of Hiyagon and Ozima, 1986). However, Ar physically adsorbed to surfaces and fractures may increase this considerably (Roselieb et al., 1997; Brooker et al., 1998a). Given these considerations, our results imply that many high-pressure experimental capsules contain sufficient inadvertently loaded Ar to allow partitioning measurements to be made by UVLAMP. Finally, we note that bulk Kr contents are consistent with modeled and measured solubilities in the starting glass (~40 ppm) without the excess observed for Ar. Contamination from air (Ar > Kr × 10^4), and presumably the welding gas, would not be detectable against the high concentration loaded with the starting material.

As illustrated in Figure 3 and Table 3, measurements of Ar contents of crystals are subject to error because of the presence of Ar-rich glass, fluid inclusions, or both. Although these can be identified at the polished sample surface before analysis (and avoided), subsurface inclusions clearly contributed to measured Ar contents in many cases. Inclusions present at depth within a pit can be identified during ablation of sequential layers as a high-concentration spike compared with lower values in previ-

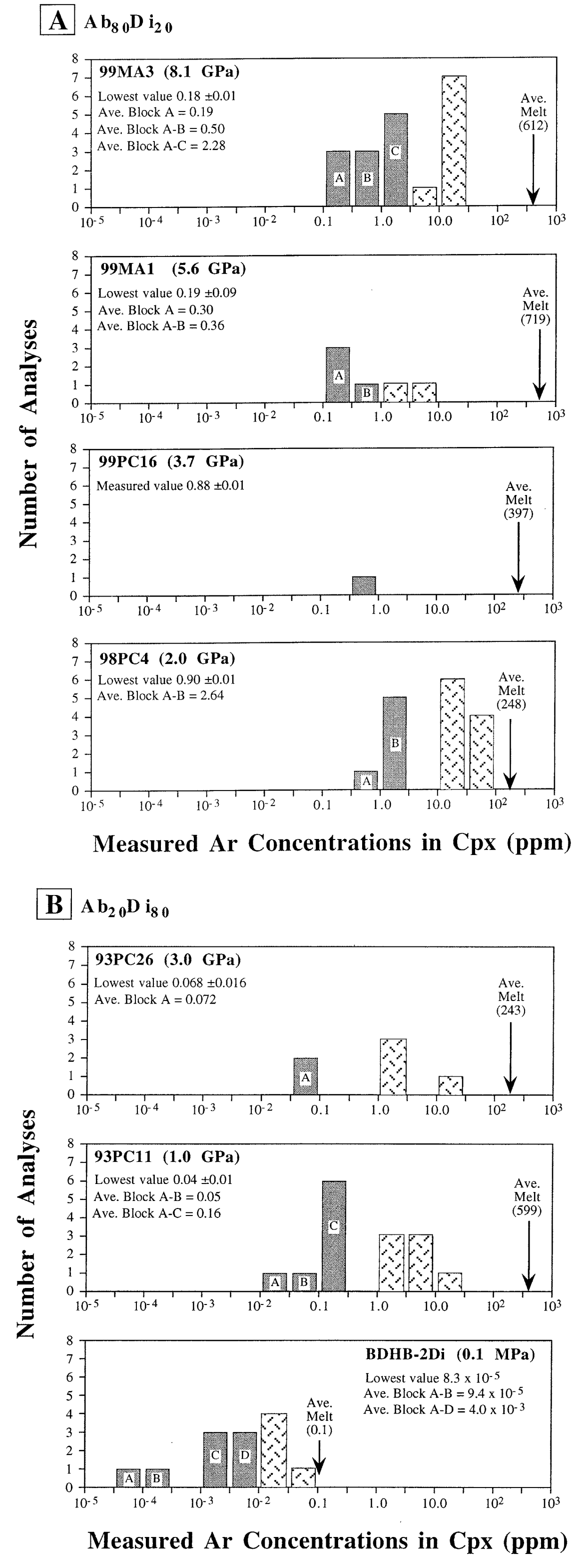

Fig. 3. The full range of Ar contents determined for clinopyroxene (cpx) crystals in (A) the $Ab_{80}Di_{20}$ system and (B) the $Ab_{20}Di_{80}$ system (including the Di-rich sample of Brooker et al., 1998a). Hatched blocks represent crystal analyses with identified inclusions of glass. Blocks marked C and D are analyses where inclusions were not identified but are believed to be present. Blocks A and B appear to represent inclusion-free data.

Table 4. Argon partition coefficients.

Sample	Crystal quality	Pressure (GPa)	Partition coefficient based on inclusion-free analyses[a]	
			Average ± error[b]	Range
D_{Ar} for $Ab_{80}Di_{20}$ system				
98PC4	Poor	2.0	0.01069 ± 0.00590	0.00036–0.01721
99PC16	Very poor	3.7	0.00222 ± 0.00055	One analysis
99MA1	Very good	5.6	0.00050 ± 0.00034	0.00026–0.00079
99MA3	Very good	8.1	0.00082 ± 0.00052	0.00029–0.00139
D_{Kr} for $Ab_{80}Di_{20}$ system				
99MA6	Very good	5.6	0.00041 ± 0.00013	0.00025–0.00051
99MA7	Very good	8.1	0.00077 ± 0.00053	0.00011–0.00155
D_{Ar} for $Ab_{20}Di_{80}$ system[c]				
BDHB-2Di[c]	Moderate	0.0001	0.00091 ± 0.00050	0.00008–0.00097
93PC11	Good	1.0	0.00008 ± 0.00004	0.00007–0.00010
93PC26	Poor to moderate	3.0	0.00030 ± 0.0003	0.00028–0.00031

[a] Based on group A and B in Fig. 3 and Table 3, or equivalent treatment of data for other samples.
[b] Errors quoted represent the analytical uncertainties from mass spectrometer analysis, the uncertainty in the measurement of the laser pit depths and volumes (± 0.5 μm), and the uncertainty in the specific densities of the material (± 5% for melt and quench material and 10% for clinopyroxene).
[c] Also including data of Brooker et al. (1998a).

ous and subsequent layers. Crystal analyses thought to be contaminated by glass inclusions are indicated in the histograms of Figure 3. It is also easier to obtain higher quality analyses on larger crystals that allow more numerous and larger ablation pits and generally contain fewer inclusions. The quality and size of crystals is indicated in Tables 3 and 4, and examples are shown in Figure 1. As can be seen in Figure 3, glass inclusions can easily raise the apparent Ar contents of crystals by more than two orders of magnitude even when the UVLAMP technique is used. It is clear that physical separation of phases coupled with bulk analysis would only exacerbate the problem.

To estimate the Ar contents of the crystals, we have rejected all analyses that we believe to be contaminated by glass inclusions, but we show all data, including glass-contaminated analyses, in Figure 3. The Ar concentrations identified as groups A and B in Figure 3 give the lowest values and appear to be uncontaminated. In some cases, a third group (C and D) has been highlighted, which we believe may be contaminated with small (unidentified) volumes of glass. The Ar concentrations and partition coefficients shown in Tables 3 and 4 are based on groups A and B only. Similar procedures were followed to obtain Kr values for two experiments at 5.6 and 8.1 GPa in the $Ab_{80}Di_{20}$ system (Tables 3 and 4). The D_{Kr} values obtained in these experiments are comparable with the D_{Ar} data for this system at the same pressure, both in terms of the limited range of values (due to similar high-quality crystals) and the absolute values.

Figure 4 shows the clinopyroxene-melt Ar partition coefficients measured in this study compared with earlier 0.1 MPa data of Broadhurst et al. (1990) and Brooker et al. (1998a) as well as the 1.5-GPa experiment of Hiyagon and Ozima (1982). All of the $Ab_{80}Di_{20}$ experimental products at 2.0 to 8.1 GPa, the 1.0- to 3.0-GPa $Ab_{20}Di_{80}$ samples, and the 0.1-MPa data of Brooker et al. (1998a) indicate highly incompatible behavior ($D_{Ar} \ll 1$) with the most reliable analyses (best-quality crystals; Table 4) having D_{Ar} values at or less than 10^{-3}. It is clear that studies that use a microprobe technique (this study and Brooker et al., 1998a) can achieve much lower D_{Ar} values than those that involve physical separation of crystals and melt and analysis of the separated bulk phase. As demonstrated in our study, inclusions within the separated crystals appear to be virtually unavoidable, leading to anomalous high D values or even values greater than one if fluid inclusions are present (Hiyagon and Ozima, 1986).

We were unable to determine D_{Ar} at pressures greater than 3 GPa in the $Ab_{20}Di_{80}$ system because repeated attempts to grow clinopyroxene at 5 to 8 GPa failed to produce crystals large enough for reliable Ar analysis. However, consideration of the partitioning data in the context of the lattice strain model (see Discussion) appears to favor similar partitioning values at all pressures in both $Ab_{80}Di_{20}$ and $Ab_{20}Di_{80}$ systems.

The general consistency of data within each compositional series, and the agreement with the 0.1 MPa measurements of Brooker et al. (1998a) for the BDHB-2Di composition (Table 4), implies that partitioning is not a disequilibrium effect controlled by adsorption or crystal dislocations. If adsorption were important, we would expect to find scattered and irreproducible behavior related to the different growth rates. Dislocations should not be significant for a strain-free crystal surrounded by a hydrostatic medium such as a melt, and it would be surprising if high, but reproducible, dislocation densities were found in experiments conducted in different apparatus over a wide range in conditions. Significantly, the measured D_{Ar} values at lower pressures (where crystal compositions are all relatively Di rich) are virtually identical even though the database covers a variation of over three orders of magnitude in Ar concentration (Fig. 3). Navrotsky (1978) has argued that the spatial constraints of dislocations make them highly selective in the size of captured ions, it thus follows that these sites would be also be selective for noble gases, favoring either Ar or Kr. Surface adsorption during crystal growth might also lead to nonequilibrium concentrations of noble gases, but the energetics of this process suggest that the heaviest noble gases (i.e., Kr and Xe) would be preferentially incorporated (see Niedermann and Eugster, 1992). As demonstrated below, the observed D_{Ar} and D_{Kr} systematics are far more consistent with an equilibrium process, such as lattice site control.

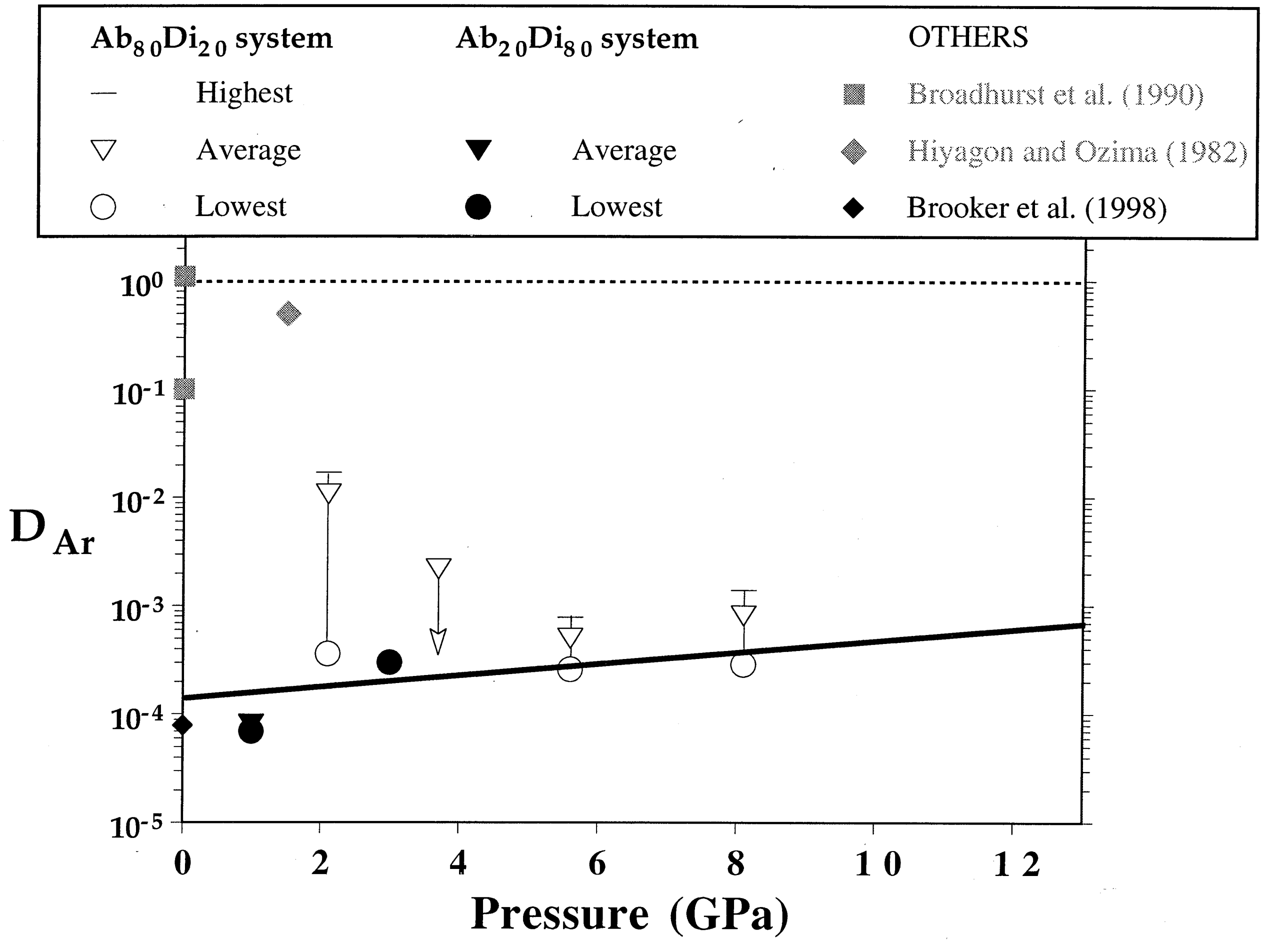

Fig. 4. Measured Ar partition coefficients (D_{Ar}) as a function of pressure. The lowest, average, and highest values correspond to the data in Table 4 and blocks A and B in Figure 3. The data point indicated with an arrow is considered a maximum value due to the poor crystal quality, and the arrow indicates the likely direction of the true partition value. The solid line is a fit to the lowest values for both systems. The Broadhurst et al. (1990) data are for melts in the CMAS system with Di-rich clinopyroxene and include the melt composition used in the Brooker et al. (1998a) study. The Hiyagon and Ozima (1982) data is for a basalt with Di-rich clinopyroxene, and these authors acknowledge that this is a maximum value due to melt contamination in the crystals.

The ion probe data for K and Rb in both phases are listed in Table 5, and partitioning values are plotted in Figure 5. Compared with the UVLAMP technique, the volume of an ion probe analysis (typically 15 × 15–μm pits, 2 to 5 μm deep) is much smaller and barely penetrates the surface, which is carefully selected to be free of melt inclusions. Consequently, the crystal analyses are far less likely to be subject to melt contamination. Where size permitted, crystals were also examined for zonation, which was found to be insignificant. The compositional and pressure related trends for these elements are very different for the $Ab_{80}Di_{20}$ and $Ab_{20}Di_{80}$ systems, as discussed below. The lack of zonation and the general agreement with predictions of the lattice strain model are again taken as evidence of equilibrium for these trace elements.

4. DISCUSSION

Table 5 and Figure 5 show ion-microprobe measurements of K and Rb partitioning between clinopyroxene and glass samples of this study, together with data from Blundy and Dalton (2000) and Blundy and Wood (1994). There are clearly contrasting, pressure-related trends for the two starting compositions. In the $Ab_{80}Di_{20}$ system, D_K and D_{Rb} decrease slightly with the initial increase in pressure before reaching near-constant values at all higher pressures. In contrast, D_K and D_{Rb} in the $Ab_{20}Di_{80}$ system follow the behavior of D_{Na}.

As discussed extensively elsewhere (e.g., Blundy and Wood, 1994; Wood and Blundy, 2001), the partitioning of cations onto crystal sites in minerals is controlled by pressure, temperature, and composition. At near-constant crystal and melt composition, partitioning is purely a function of pressure and temperature. Blundy et al. (1995) showed that this simple relationship can be reconciled in terms of the melting behavior of an end-member crystal component containing the ion or ions of interest. Thus, the partitioning of Na between clinopyroxene and silicate melt can be modeled by using the fusion thermodynamics of jadeite (see Blundy et al., 1995). Partitioning of

Table 5. Potassium and rubidium partitioning data.[a]

Sample	Melt K (ppm)	Cpx K (ppm)	D_K	Melt Rb (ppm)	Cpx Rb (ppm)	D_{Rb}
$Ab_{80}Di_{20}$ system						
98PC2	533 ± 1	7.2 ± 0.4	0.0135 ± 0.0008	391 ± 6	0.152 ± 0.021	0.000389 ± 0.000111
99MA1	1394 ± 25	9.3 ± 1.0	0.0067 ± 0.0007	1174 ± 47	0.097 ± 0.007	0.000083 ± 0.000007
99MA3	1089 ± 60	12.4 ± 1.6	0.0114 ± 0.0016	766 ± 78	0.120 ± 0.006	0.000157 ± 0.000018
99MA6	658 ± 3	7.1 ± 0.3	0.0108 ± 0.0005	512 ± 5	0.091 ± 0.006	0.000178 ± 0.000012
99MA7	1659 ± 79	10.6 ± 1.3	0.0064 ± 0.0008	1400 ± 154	0.124 ± 0.033	0.000089 ± 0.000025
$Ab_{20}Di_{80}$ system[b]						
BDHB-2Di[b]	11040 ± 1300	<100	<0.0091			
93PC11	402 ± 25	4.9 ± 3.2	0.0122 ± 0.008	228 ± 12	0.130 ± 0.081	0.000570 ± 0.000352
93PC26	257 ± 43	2.2 ± 0.6	0.0086 ± 0.0029	157 ± 27	0.201 ± 0.090	0.001270 ± 0.000610
93MA1[c]	311 ± 83	39 ± 12	0.1250 ± 0.0518	89 ± 44	1.300 ± 0.400	0.015 ± 0.008
BW17	350 ± 54	107 ± 14	0.3063 ± 0.0622	537 ± 207	18.23 ± 6.00	0.034 ± 0.017

[a] Quoted error for concentrations is 1 standard deviation based on two to three analyses.
[b] Also including data of Brooker et al. (1998a). Concentrations determined by electron probe. Cpx data revised from value in original publications.
[c] Sample from Blundy et al. (1995). Cpx too small for Ar analyses.

other cations of the same charge, entering the same site (e.g., K, Rb, Cs) will show similar behavior. In detail, the partition coefficients for K, Rb, and Cs can be related to D_{Na} via the lattice strain model of Blundy and Wood (1994), whereby the controlling factor is the energy required to insert a misfit cation into a crystal lattice site. Because K, Rb, and Cs, are all larger than Na, this energy is positive, and all three cations have smaller D values than Na, decreasing in order of increasing ionic radius (i.e., $D_K > D_{Rb} > D_{Cs}$). As temperature (and lattice vibration) increases, the energy required to accommodate misfit ions decreases, so that partition coefficients approach the same value for all ions at infinite temperature. In the system $Ab_{20}Di_{80}$ (Fig. 5B), these three key features of the lattice strain model are observed: (1) with increasing pressure, D_K and D_{Rb} are parallel to D_{Na}; (2) $D_{Na} > D_K > D_{Rb}$; and (3) D_{Na}/D_K and D_K/D_{Rb} decrease with increasing temperature (note that increasing temperature is associated with increasing pressure in our experiments). This observation is primarily a consequence of the near-constant clinopyroxene crystal chemistry in this system. The D_K pressure trend in Figure 5B is also consistent with the data for diopside-rich clinopyroxene in 2- to 8-GPa experiments that use various natural starting compositions (Lloyd et al., 1985; Edgar and Vukadinovic, 1993; Edgar and Mitchell, 1997).

The situation in the $Ab_{80}Di_{20}$ system involves the complexity of changes in clinopyroxene composition in addition to variable pressure and temperature. Clinopyroxene composition affects the optimum size of ions that can be incorporated on a site. In the case of large cations entering clinopyroxene, it is the size of the large M2 site that is important. Wood and Blundy (1997) have shown that this site is sensitive to crystal chemistry, increasing in size at higher Ca and lower octahedral Al contents. Although not explicitly discussed by Wood and Blundy (1997), the M2 site should also decrease in size with increasing Na content, in keeping with the small M2-O bond lengths in jadeite relative to diopside (Smyth and Bish, 1988). This decrease in the size of M2 will favor incorporation of smaller ions such as Na^+ over larger ions such as Rb^+. It is the effect of increasing jadeite content with pressure that accounts for the disparate partitioning behavior of K, Rb, and Na in the $Ab_{80}Di_{20}$ as compared with the $Ab_{20}Di_{80}$ system (Figs. 5A, B). In the $Ab_{80}Di_{20}$ system, compositional changes counteract the pressure and temperature effects, and as a result there is no increase in D_K and D_{Rb} with increasing pressure and temperature (cf. Fig. 5B).

The lattice strain model is also able to account for the observed partitioning behavior of the noble gases, Ar and Kr. As first demonstrated by Blundy and Wood (1994), the tendency for lattice sites to discriminate against misfit cations (i.e., those that are larger or smaller than the optimum site radius) decreases as the charge of the substituent ion decreases. A logical extension of this simple observation is that the noble gases, with effective zero charge, should not be discriminated against by lattice sites on account of the size (Wood and Blundy, 2001). Thus, a first-order prediction of the lattice strain model is that noble gases substituting on lattice sites should show essentially the same partition coefficient, irrespective of their atomic radius. In practice, it is likely that this prediction will only hold for the larger noble gases, because smaller atoms, such as He and possibly Ne, may be located on the smaller M1 site or in interstitial locations. The first-order prediction for the heavy noble gases is borne out by our data for D_{Ar} and D_{Kr}, which are almost identical (within error) in Figure 5A. This partitioning behavior is similar despite a considerable difference in atomic radius of Ar and Kr (1.77 vs. 1.87 Å; Zhang and Xu, 1995), which is comparable to that of K and Rb (1.51 vs. 1.61 Å; Shannon, 1976). Furthermore, the lattice strain model predicts that for neutral atoms, whose partitioning is size independent, there should be considerably less dependence on crystal chemistry than for more highly charged species. We suggest that this would account for the near-constancy of D_{Ar} in all run products, irrespective of crystal composition (solid line in Fig. 4).

In conclusion, the partitioning behavior of Na, K, and Rb are consistent with previous experimental studies on alkali partitioning between clinopyroxene and melt in the Ab-Di system (e.g., Blundy and Wood, 1994; Blundy et al., 1995) and can be explained in terms of the lattice strain model. The partitioning behavior of Ar and Kr is consistent with a simple extrapolation of the cation partitioning data to neutral species. This consistency provides further compelling evidence that Ar and Kr reside in the lattice sites of clinopyroxene in our experiments.

The results of this study confirm the conclusions of Brooker et al. (1998a): that D_{Ar} between clinopyroxene and silicate melt

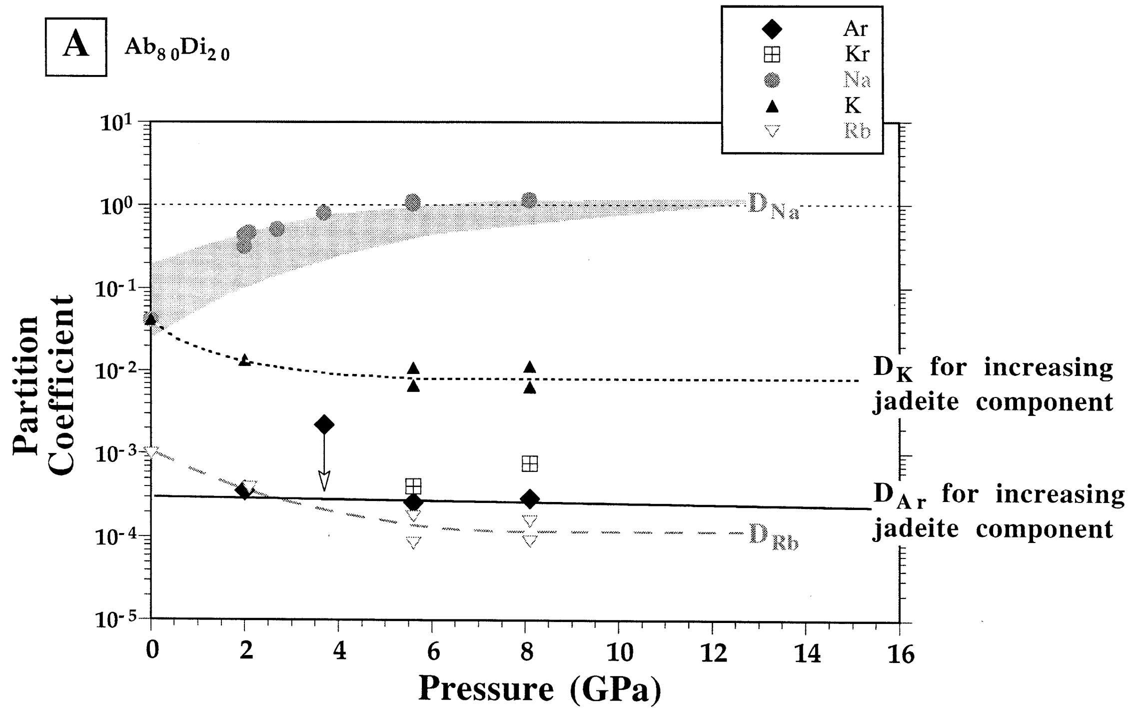

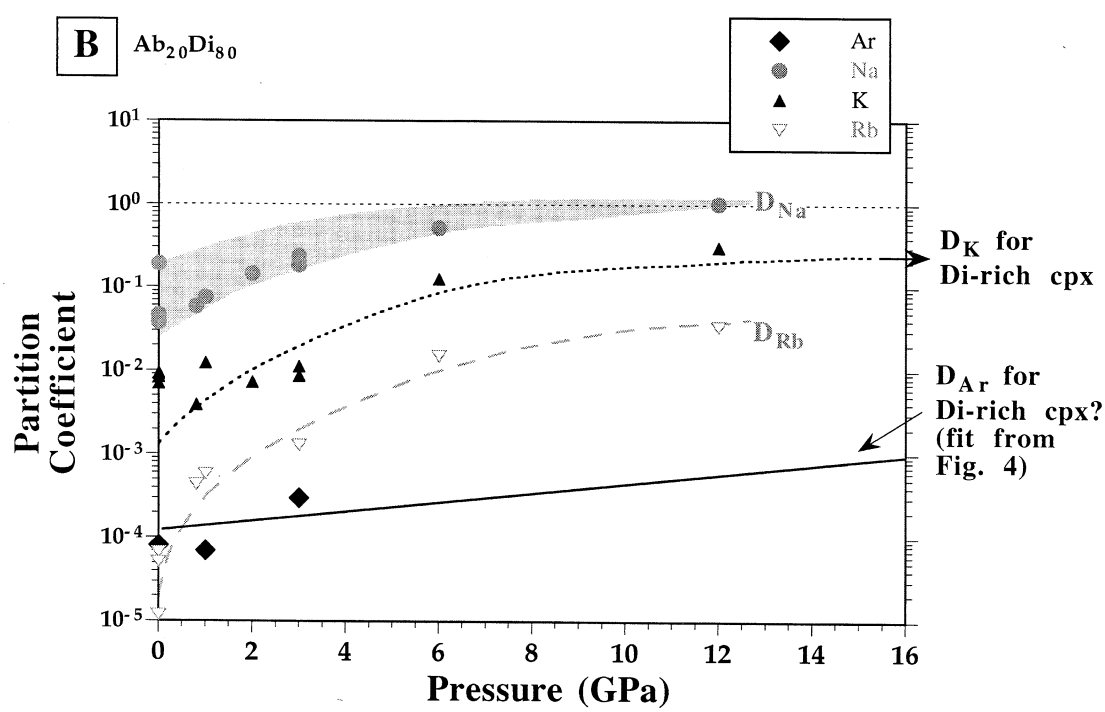

Fig. 5. Comparison of D_{Na}, D_K, D_{Rb}, and D_{Ar} as a function of pressure for (A) the $Ab_{80}Di_{20}$ system and (B) the $Ab_{20}Di_{80}$ system (including the Di-rich samples of Brooker et al., 1998a). It should be noted that the experimental temperature also increasing with pressure (Table 1). The D_{Kr} values determined in this study are also included in (A). D_{Na}, D_K, and D_{Rb} for additional $Ab_{20}Di_{80}$ samples of Blundy et al. (1995) are also shown. The shaded area covers all the D_{Na} data for both systems. The dotted curves through the K and Rb data are fitted in (A) but are drawn approximately subparallel to the D_{Na} trend in (B) (i.e., not a fit to the data). The solid line in (A) represents a fit through the three best D_{Ar} data points for the $Ab_{80}Di_{20}$ system. The solid line in (B) is the fit to all the D_{Ar} data as in Figure 4 but closely coincides with a fit to the $Ab_{20}Di_{80}$ data points.

is very low, in contrast to previous determinations that have used bulk analytical techniques. These low D_{Ar} values ($<10^{-3}$) appear to be constant up to pressures of at least 3 to 4 GPa and for a range of clinopyroxene compositions, including the Di-rich compositions relevant to mantle assemblages.

The most important mechanism for mantle degassing is probably melting beneath midocean ridges (MOR), which is thought to occur to a depth of 60 or 100 km. A small but significant contribution may be related to hot-spot melting, generated as plume material rises to approach similar depths. It is the transfer of these melts to the surface that leads to removal of noble gases from the mantle system. Consequently, the crystal-melt partition coefficients operating in a spinel or garnet lherzolite phase assemblage at pressures to ~4 GPa represents one of the dominant controls in the evolution of noble gas distributions and chemical geodynamics. As can be seen in Figure 5, D_K for clinopyroxene is in the range 6×10^{-3} to 1.4×10^{-2} at pressures less than 4 GPa. Clinopyroxene is the only significant potassium host in a normal (anhydrous) MOR basalt source region, and as generally assumed in the literature (e.g., Hofmann, 1988), K will be extremely incompatible (bulk $D_K \approx 10^{-4}$) during melting for a typical residual assemblage (olivine, orthopyroxene, spinel, or garnet with or without clinopyroxene). The values of D_{Ar} presented for clinopyroxene in this study (Fig. 5) might be taken to indicate that K is substantially more compatible than Ar in the mantle over the relevant pressure range ($D_K \geq 10 \times D_{Ar}$). However, the D_{Ar} as measured by UVLAMP for olivine experimentally grown in simple or natural melt systems (Brooker et al., 1998a) and careful bulk measurements for natural basalts (Marty and Lussiez, 1993; Valbracht et al., 1994) are all close to 10^{-2}. This value is significantly higher than the D_{Ar} for clinopyroxene, suggesting that the electrostatic energy (as described in Wood and Blundy, 2001) associated with incorporation of neutral atoms on M1 and/or M2 site in olivine, is less than in clinopyroxene. This effect can be anticipated from the olivine trace element partitioning data of Taura et al. (1998) for 1^+, 2^+, and 3^+ cations extrapolated to a neutral (zero charge) atom by means of the method of Wood and Blundy (2001). The predicted D_{Ar} of 0.02 to 0.04 for olivine at 3 GPa is consistent with the data of Brooker et al. (1998a).

In modal terms, olivine is the most abundant mineral in both fertile and depleted lherzolite. The other abundant mineral, opx, contains similar lattice sites to olivine and may therefore show similar partitioning behavior for noble gases and K. As a result, the bulk D_{Ar} for the upper mantle could be close to 10^{-2}. This is higher than the initial bulk D_K for melting of fertile lherzolite, which is controlled solely by clinopyroxene. However, K will be lost as clinopyroxene is melted out, leaving a very low K/Ar ratio in a clinopyroxene-free residue. Thus, it would appear that models of shallow mantle degassing can be based on the assumption that both K and Ar are reasonably incompatible, but the commonly held view that K is substantially more compatible than Ar may not be true. As a result, the idea that all primordial Ar (^{36}Ar and ^{38}Ar) has been stripped from the upper mantle layer, to be replaced by radiogenic ^{40}Ar grown from residual ^{40}K, may be oversimplified. The residual K/Ar ratio will be highly variable depending on the amount of clinopyroxene left after melting, being very low in harzburgite, which has no host for K but retains some Ar. If isolated for some time, this could lead to a locally heterogeneous distribution of $^{40}Ar/^{36}Ar$ ratios. Variations in this ratio are commonly observed in MOR basalts but are usually attributed to differing degrees of atmospheric contamination arising from mixing of a subducted component, or interaction with seawater during eruption. Obviously, some sections of the mantle may remain relatively K rich and fertile by escaping repeated melt extraction for extended periods of time or being subject to refertilized by high K/Ar material (subducted crust?). These regions will develop relatively high $^{40}Ar/^{36}Ar$ ratios, irrespective of whether they are confined to a lower undegassed reservoir, or remain as slightly degassed heterogeneities in the upper mantle, lower mantle, or both. However, regions of K-rich, fertile mantle are more likely to melt when reintroduced to a shallow melt zone. This may give a false impression of the bulk $^{40}Ar/^{36}Ar$ ratio in the upper mantle.

Acknowledgments—We thank the EC for the award of a Marie Curie Fellowship (E.M.C.), Bruno Reynard for confirming the presence of coesite by Raman spectroscopy, and Jon Craven for help in obtaining ion probe data. J.D.B. thanks the Royal Society for provision of a research fellowship. We also thank Chris Ballentine, Dave Draper, Bjorn Mysen, and an anonymous reviewer for their constructive comments.

Associate editor: B. Mysen

REFERENCES

Allègre C. J., Staudacher T., and Sarda P. (1987) Rare gas systematics: Formation of the atmosphere, evolution and structure of the Earth's mantle. *Earth Planet. Sci. Lett.* **81,** 127–150.

Allègre C. J., Hofmann A., and O'Nions K. (1996) The Argon constraints on mantle structure. *Geophys. Res. Lett.* **23,** 3555–3557.

Anderson D. L. (1993) Helium-3 from the mantle: Primordial signature or cosmic dust? *Science* **261,** 170–176.

Batiza R., Bernatowicz T. J., Hohenberg C. M., and Podosek F. A. (1979) Relations of noble gas abundances to petrogenesis and magmatic evolution of some oceanic basalts and related differentiated volcanic rock. *Contrib. Min. Petrol.* **69,** 301–313.

Blundy J. D. and Wood B. J. (1994) Predictions of crystal-melt partition coefficients from elastic moduli. *Nature* **372,** 452–454.

Blundy J. D., Fallon T. J., Wood B. J., and Dalton J. A. (1995) Sodium partitioning between clinopyroxene and silicate melts. *J. Geophys. Res.* **100,** 15., 501–15,515.

Blundy J. D., Robinson J. A. C., and Wood B. J. (1998) Heavy REE are compatible in clinopyroxene on the spinel lherzolite solidus. *Earth Planet. Sci. Lett.* **160,** 493–504.

Blundy J. and Dalton J. (2000) Experimental comparison of trace element partitioning between clinopyroxene and melt in carbonate and silicate systems, and implications for mantle metasomatism. *Contrib. Mineral. Petrol.* **139,** 356–371.

Brice J. C. (1975) Some thermodynamic aspects of the growth of strained crystals. *J. Crystal Growth* **28,** 249–253.

Broadhurst C. L., Drake M. J., Hagee B. E., and Bernatowicz T. J. (1990) Solubility and partitioning of Ar in anorthite, diopside, forsterite, spinel, and synthetic basaltic liquids. *Geochim. Cosmochim. Acta* **54,** 299–309.

Broadhurst C. L., Drake M. J., Hagee B. E., and Bernatowicz T. J. (1992) Solubility and partitioning of Ne, Ar, Kr, and Xe in minerals and synthetic basalt melts. *Geochim. Cosmochim. Acta* **56,** 709–723.

Brooker R. A., Wartho J-A., Carroll M. R., Kelley S. P., and Draper D. S. (1998a) Preliminary UVLAMP determinations of argon partition coefficients for olivine and clinopyroxene grown from silicate melts. *Chem. Geol.* **147,** 185–200.

Brooker R. A., Holloway J. R., and Hervig R. L. (1998b) Reduction in piston cylinder experiments: The detection of carbon infiltration into platinum capsules. *Am. Mineral.* **83,** 985–994.

Carroll M. R. and Stolper E. M. (1993) Noble gas solubilities in silicate melts and glasses: New experimental results for Ar and the relationship between solubility and ionic porosity. *Geochim. Cosmochim. Acta* **57,** 5039–5051.

Chamorro-Perez E., Gillet P., and Jambon A. (1996) Argon solubility in silicate melts at very high pressures. Experimental set-up and preliminary results for anorthite and silica melts. *Earth Planet. Sci. Lett.* **145,** 97–107.

Chamorro-Perez E., Gillet P., Jambon A., Badro J., and McMillan P. (1998) Low argon solubility in silicate melts at high pressure. *Nature* **393,** 352–355.

Coltice N. and Ricard Y. (1999) Geochemical observations and one layer mantle convection. *Earth Planet. Sci. Lett.* **174,** 125–137.

Coltice N., Albarède F., and Gillet P. (2000) ^{40}K-^{40}. Ar constraints on recycling continental crust into the mantle. *Science* **288,** 845–847.

Davies G. F. (1999) Geophysically constrained mantle mass flows and the ^{40}Ar budget: A degassed lower mantle? *Earth Planet. Sci. Lett.* **166,** 149–162.

Deer W. A., Howie R. A. and Zussman J. (1992) *An Introduction to the Rock-Forming Minerals.* 2nd ed. Longman Scientific.

Edgar A. D. and Vukadinovic D. (1993) Potassium-rich clinopyroxene in the mantle: An experimental investigation of a K-rich lamproite up to 60 kbar. *Geochim. Cosmochim. Acta* **57,** 5063–5072.

Edgar A. D. and Mitchell R. H. (1997) Ultra high pressure-temperature melting experiments on a SiO_2-rich lamproite from Smoky Butte, Montana: Derivation of siliceous lamproite magmas from enriched sources deep in the continental mantle. *J. Petrol.* **38,** 457–477.

Harmano Y. and Ozima M. (1978) Earth-atmosphere evolution model based on Ar isotopic data. In *Terrestrial Rare Gases* (eds. E. C. Alexander Jr. and M. Ozima), pp. 155–171. Jpn. Sci. Soc. Press, Tokyo.

Harper L. C. and Jacobsen S. B. (1996) Noble gases and Earth's accretion. *Science* **273,** 1814–1818.

Hart R., Hogan L., and Dymond G. (1985) The closed-system approximation for evolution of argon and helium in the mantle, crust and atmosphere. *Chem. Geol.* **52,** 45–73.

Hiyagon H. and Ozima M. (1982) Noble gas distribution between basalt melt and crystals. *Earth Planet. Sci. Lett.* **58,** 255–264.

Hiyagon H. and Ozima M. (1986) Partition of noble gases between olivine and basalt melt. *Geochim. Cosmochim. Acta* **50,** 2045–2057.

Hofmann A. W. (1988) Chemical differentiation of the earth: The relationship between mantle, continental crust and oceanic crust. *Earth Planet. Sci. Lett.* **90,** 297–314.

Hofmann A. W. (1997) Mantle chemistry: The message from oceanic volcanism. *Nature* **385,** 219–229.

Jambon A. (1994) Earth degassing and large-scale geochemical cycling of volatile elements. *Rev. Mineral.* **30,** 479–517.

Kaneoka I., Takaoka N., and Clague D. A. (1983) Noble gas sytematics for coexisting glass and olivine crystals in basalt and dunite xenoliths from Loihi Seamount. *Earth Planet. Sci. Lett.* **66,** 427–437.

Kelley S. P., Arnaud N. O., and Turner S. P. (1994) High spatial resolution ^{40}Ar/^{39}Ar investigations using an ultra-violet laser probe extraction technique. *Geochim. Cosmochim. Acta* **58,** 3519–3525.

Kurz M. D., Jenkins W. J., Schilling J. G., and Hart S. R. (1982) Helium isotope systematics of oceanic islands Helium isotopic variations in the mantle beneath the central North Atlantic Ocean. *Earth Planet. Sci. Lett.* **58,** 1–14.

Landwehr D., Blundy J., Chamorro-Perez E. M., Hill E., and Wood B. J. (2001) U-series disequilibria generated by partial melting of spinel lherzolite. *Earth Planet. Sci. Lett.* **188,** 329–348.

Lange R. M. and Carmichael I. S. E. (1987) Densities of Na_2O-K_2O-CaO-MgO-FeO-Fe_2O_3-Al_2O_3-TiO_2-SiO_2 liquids: New measurements and derived partial molar properties. *Geochim. Cosmochim. Acta* **51,** 2931–2946.

Lloyd F. E., Arima M., and Edgar A. D. (1985) Partial melting of a phlogopite–clinopyroxenite nodule from south-west Uganda: An experimental study bearing on the origin of highly potassic continental rift volcanics. *Contrib. Mineral. Petrol.* **91,** 321–329.

Marty B. and Lussiez P. (1993) Constraints on rare gas partition coefficients from analysis of olivine-glass from a picritic mid-ocean ridge basalt. *Chem. Geol.* **106,** 1–7.

McKenzie D. and O'Nions R. K. (1991) Partial melt distributions from inversion of rare earth element concentrations. *J. Petrol.* **23,** 1021–1091.

Nagasawa H. (1966) Trace element partition coefficients in ionic crystals. *Science* **152,** 767–769.

Navrotsky A. (1978) Thermodynamics of element partitioning: (1) Systematics of transition metals in crystalline and molten silicates, and (2) defect chemistry and "The Henry's Law Problem." *Geochim. Cosmochim. Acta* **42,** 887–902.

Niedermann S. and Eugster O. (1992) Noble gases in lunar anorthositic rocks 60018 and 65315: Acquisition of terrestrial krypton and xenon indicating an irreversible adsorption process. *Geochim. Cosmochim. Acta* **56,** 493–509.

O'Nions R. K. and Tolstikhin I. N. (1996) Limits on the mass flux between lower and upper mantle and stability of layering. *Earth Planet. Sci. Lett.* **139,** 213–222.

Ozima M. and Podosek F. A. (1983) *Noble Gas Geochemistry*. Cambridge University Press.

Ozima M. and Igarashi G. (2000) The primordial noble gases in the Earth: A key constraint on Earth evolution models. *Earth Planet. Sci. Lett.* **176,** 219–232.

Phipps-Morgan J. and Morgan W. J. (1999) Two-stage melting and the geochemical evolution of the mantle: A recipe for mantle plum-pudding. *Earth Planet. Sci. Lett.* **170,** 215–239.

Porcelli D. and Wasserburg G. J. (1995) Mass transfer of helium, neon, argon, and xenon through a steady-state upper mantle. *Geochim. Cosmochim. Acta* **59,** 4921–4937.

Roselieb K., Blanc P., Buttner H., Jambon A., Rammensee W., Rosenhauer M., Vielzeuf D. and Walter H. (1997) Experimental study of argon sorption in quartz: Evidence for argon incompatibility. *Geochim. Cosmochim. Acta* **61,** 533–542.

Shannon R. D. (1976) Revised effective radii and systematic studies of interatomic distances in halides and chalcogenides. *Acta Cryst. A* **32,** 751–767.

Shibata T., Takahashi E., and Ozima M. (1994) Noble gas partitioning between basaltic melt and olivine crystals at high pressures. In *Noble Gas Geochemistry and Cosmochemistry*. (ed. J.-I. Matsuda), pp. 343–354. Terra Science Publishing.

Smyth J. R. and Bish D. L. (1988) *Crystal Structures and Cation Sites of the Rock Forming Minerals.* 59 Allen & Unwin.

Taura H., Yurimoto H., Kurita K., and Sueno S. (1998) Pressure dependence on partition coefficients for trace elements between olivine and coexisting melts. *Phys. Chem. Mineral.* **25,** 469–484.

Turner G. (1989) The outgassing history of the Earth's atmosphere. *J. Geol. Soc. Lond.* **146,** 147–154.

Valbracht P. J., Honda M., Staudigel H., McDougall I., and Trost A. P. (1994) Noble gas partitioning in natural samples: Results from coexisting glass and olivine phenocrysts in four Hawaiian submarine basalts. In *Noble Gas Geochemistry and Cosmochemistry* (ed. J.-I. Matsuda), pp. 373–381. Terra Science Publishing.

van der Hilst R. D., Widiyantoro S., and Engdahl E. R. (1997) Evidence for deep mantle circulation from global tomography. *Nature* **386,** 578–584.

van Keken P. F. and Ballentine C. J. (1999) Dynamical models of mantle volatile evolution and the role of phase transitions and temperature-dependent rheology. *J. Geophys. Res.* **104,** 7137–7151.

Walker D., Carpenter M. A. and Hitch C. M. (1990) Some simplifications to multianvil devices for high pressure experiments. *Am. Mineral.* **75,** 1020–1028.

Wartho J.-A., Kelley S. P., Brooker R. A., Carroll M. R., Villa I. M., and Lee M. R. (1999) Direct measurement of argon diffusion profiles in a gem-quality Madagascar K-feldspar using the ultra-violet laser ablation micro-probe (UVLAMP). *Earth Planet. Sci. Lett.* **170,** 141–153.

Wood B. J. and Blundy J. D. (1997) A predictive model for rare earth element partitioning between clinopyroxene and anhydrous silicate melt. *Contrib. Mineral. Petrol.* **129,** 166–181.

Wood B. J. and Blundy J. D. (2001) The effect of cation charge on crystal-melt partitioning of trace elements. *Earth Planet. Sci. Lett.* **188,** 59–71.

Zhang Y. and Zindler A. (1989) Noble gas constraints on the evolution of the Earth's atmosphere. *J. Geophys. Res.* **94,** 13719–13737.

Zhang Y. and Xu Z. (1995) Atomic radii of noble gas elements in condensed phases. *Am. Mineral.* **80,** 670–675.